Towards robust deconvolution of hyperspectral data cubes

Alexis Lau, Benoit Neichel, Romain Fétick, Thierry Fusco

Towards robust deconvolution of hyperspectral data cubes

Alexis Lau[a], Benoit Neichel[a], Romain Fetick[a, b], and Thierry Fusco[a,b]

[a]Aix Marseille Univ, CNRS, CNES, LAM, Marseille, France
[b]DOTA, ONERA, Université Paris Saclay, F-91123 Palaiseau, France

ABSTRACT

One crucial aspect for the science observations assisted by Adaptive Optics (AO) is the knowledge of the Point Spread Function (PSF). The PSF delivered by AO systems has a complex shape, combining spatial, spectral and temporal variability, such that its characterization is often a major limitation when analyzing AO data. The absence of reference calibrators is also common in cases like extended objects and very crowded regions. This paper presents a post-processing method (called AMIRAL) derived from blind deconvolution, which allows us to estimate the AO-PSF directly from scientific observations. AMIRAL uses an analytical PSF model (PSFAO19) and simplifies the estimation down to a few parameters. The resultant PSF is used to perform deconvolution. We first evaluate the performance of AMIRAL for PSFs retrieval with simulated data in different parameters. Then, we present a new feature by introducing a Fourier-based object model. Taking advantage of having a more realistic representation of the object, we improve both the performance and robustness of the PSF estimation, and the consequent deconvolution process. This performance gain is eventually illustrated with real observations of the asteroid Kleopatra acquired by VLT-SPHERE.

Keywords: adaptive optics, image processing, deconvolution, PSF estimation

1. INTRODUCTION

Point-Spread Function (PSF) retrieval remains a key challenge in Adaptive Optics (AO) observations. Inadequate knowledge of the PSF sets a hard limit on delivering precise photometric and astrometric data or providing any information with a higher spatial resolution. As the AO system offers partial corrections of the atmospheric turbulence, observations still suffer from blurring. When observing extended targets, deconvolution allows to enhance the image contrast and recover the fine structures of the image. It eventually opens the path for accurate topology and volume estimation of asteroids. However, deconvolution is highly sensitive to the input PSF.[1,2] Without proper PSF models, it is nearly impossible to perform this operation, even with the presence of reference PSFs.

In this proceeding, we focus on blind deconvolution as we would like to deliver a robust method that aims to reduce additional telescope times to get a reference PSF if possible. We first review current methods in section 2. Then based on current methods, we demonstrate in section 3 to what level we need to know the PSF for adequate deconvolution. Based on these requirements, we illustrate the process with simulated and science observations in section 4.

2. STATE OF THE ART FOR PSF ESTIMATION AND DECONVOLUTION

Fig .1 illustrates the impact of using a wrong PSF when performing deconvolution. In this example an image is simulated with a given PSF, and a different PSF is used for deconvolution. The subtle changes in both PSFs are not noticeable. However, it leads to a drastic difference in deconvolution. This illustrates the need for accurate PSf models, and PSF retrieval from the observations is necessary if we do not have access to the ground truth. One of the traditional ways to perform PSF retrieval from observation is blind deconvolution with joint estimator.[3] This method results in poor quality[4,5] as the solutions degenerate. The difficulties in separating the object from the PSF in the image cause the degeneracy. In the joint estimator, we need to estimate N^2 pixels from the PSF plus N^2 pixels from the object. A reduction in the number of parameters may allow us to separate the target in the image from the PSF. A more reliable approach is to use a marginal estimator with models for both the PSF and the object one would like to retrieve. To ensure a consistent estimation, methods like combining an analytical PSF model[6] and an empirical object model[7] have been developed.[4] The advantages

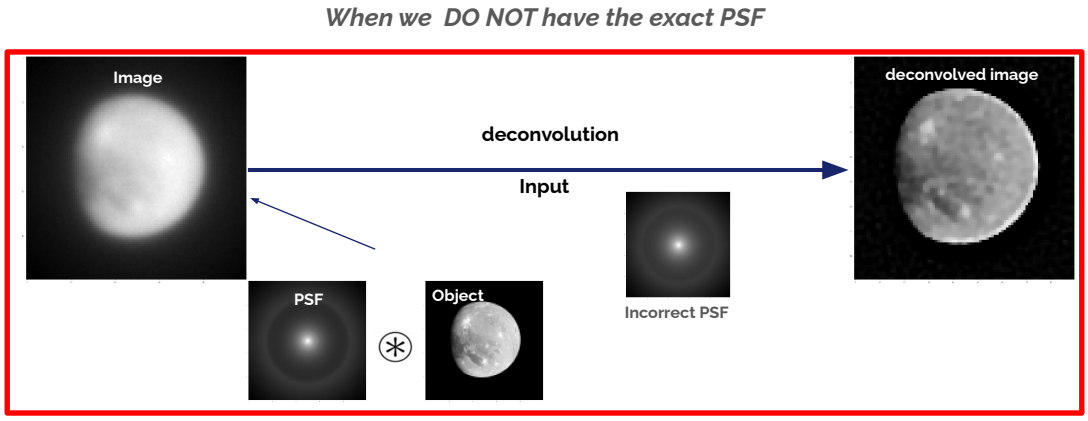

Figure 1. Schematic showing the process of deconvolution and the consequence of having a mismatch PSF. The condition might have changed rapidly during observation. Having a reference star in the field does not guarantee a useful PSF for deconvolution, as deconvolution requires accurate knowledge of the input PSF.

of introducing an analytical PSF model are (i) reducing the degree of freedom from the number of pixels of the image down to a few variables, and (ii) providing physical intuition into the process. In addition, having a physical PSF model like PSFAO19[6] allows us to incorporate additional prior information on the observing conditions if needed. For the object, an estimation of the Power Spectral Density (PSD) is required, which can be as simple as a 1D parametric function, as for instance the model proposed by Conan et al.[7] In particular, this model consists of 3 parameters: (i) noise of the image, (ii) the cut-off frequency and (iii) the slope of the PSD. Recent work[4] has shown that blind deconvolution with the marginal estimator is working well, with some limited regimes. The main issue lying in the choice of the object Power Spectrum Density (PSD) model. When moving away from circular objects, the Conan model[7] starts to fail. Based on the marginal estimator with PSF and object PSD models, we would like to expand the operational range of the current PSF estimation tool by improving the modelling of objects' PSD, such that it can accept a wider variety of objects. To expand the operational range of current PSF estimation tools for deconvolution, one must understand what accuracy is required when deconvolving astronomical images. This is often overlooked as there is no metric or ground truth to compare with when we are studying extending objects on sky.

3. DECONVOLUTION SENSITIVITY

We first acknowledge that there is no existing quantitative metric to assess the quality of the deconvolved product. Without knowing this sensitivity level, we cannot evaluate the performance of different PSF estimations method for deconvolution. Ideally, we would like have a PSF as close to the true PSF as possible. In practice, we do not have access to any ground truth. We start investigating the range that the estimated PSF needs to be in with simulated data. We made simulations with Jupiter's Moon, Ganymede from the JUNO mission,[8] and a reference PSF generated by PSFAO19 model. This high-resolution object is then binned to the size to fit the ground-based observations. We choose to investigate the tolerance with simulated data because we have the ground truths for both the estimated object and the reference PSF. This can offer an insight into the required sensitivity level. Recalling the image formation theory, we are interested in the formulation of the PSF. Roddier[9] states that for

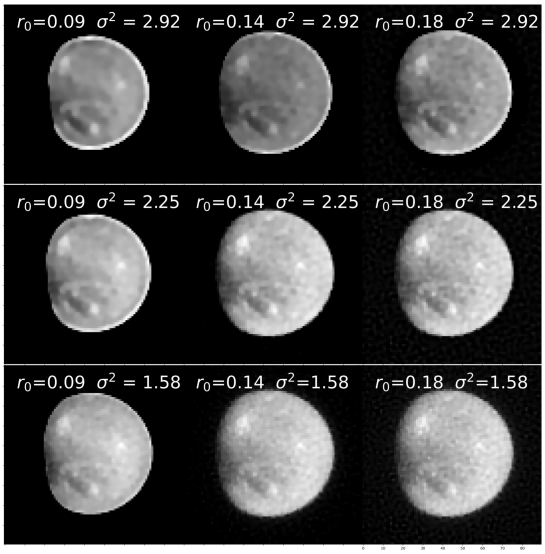

Figure 2. Visualisation of the deconvolution sensitivity with simulated data, using the Ganymede from the JUNO mission as the object. Centre: Deconvolution with the true PSF. Other cases are the deconvolutions performed with the listed PSF parameters.

long exposure frames, the convolution of the system, the telescope and the atmospheric turbulence results in the PSF,

$$h = h_A \circledast h_T \tag{1}$$

$$\tilde{h} = \tilde{h_A} \times \tilde{h_T}, \tag{2}$$

where h is the analytical PSF, $\tilde{h}_{\rm t}$ is the telescope optical transfer function (OTF), $\tilde{h}_{\rm a}$ is the atmospheric optical transfer function. The turbulent OTF comes from the phase PSD (W_ϕ)

$$W_\phi(f) = \left[\frac{\beta-1}{\pi\alpha_x\alpha_y}\frac{M_A(f_x,f_y)}{1-(1+\frac{f_{AO}^2}{\alpha_x\alpha_y})^{1-\beta}} + C\right]_{f<f_{AO}} + \left[0.023 r_0^{-5/3} f^{-11/3}\right]_{f>f_{AO}},$$

$$h(f) = \mathcal{F}^{-1}\{\tilde{h_T} e^{B_\phi(0)} e^{\mathcal{F}^{-1}\{W_\phi(f)\}}\}, \tag{3}$$

where B_ϕ is the phase auto-correlation function, $W_{\phi(f)}$ is the phase PSD, which is characterised by physical parameters: fried parameter (r_0) and phase variance (σ^2). where $\tilde{h}$ is the OTF, the Fourier transform of the PSF.[9] We then perform $l^2 - l^1$ deconvolution[3] with 225 different PSFs, varying r_0 and σ^2 by $\pm$30%. Fig. 2 demonstrates the effect of deconvolution with a range of different PSF parameters. The impact of over-and under-estimating PSF parameters for deconvolution in the fig. 2 are apparent, as we achieved better visual results with over-estimation. Regardless of the metric or a range of deconvolution sensitivity, visual inspections are required to determine whether the product is adequate. If we want to get an accurate deconvolution, then it means we at least need to know the PSF parameters within $\pm$ 30 %, as shown in fig. 2. In particular, for $r0$ and σ^2 $\pm$ 10 - 20 %. to To conclude, deconvolution should be performed by over-estimating PSF variables, minimising having too many artefacts or suffering from over- or under-deconvolution.

4. IMPROVED MODEL FOR OBJECTS IN PSF ESTIMATION

Here we adapt PSFAO19[6] and the marginal estimator 4,5 as the basis of the PSF estimation. To be more precise, our method is a two-step methodology, 1. PSF Estimation from the image, 2. Perform standard deconvolution

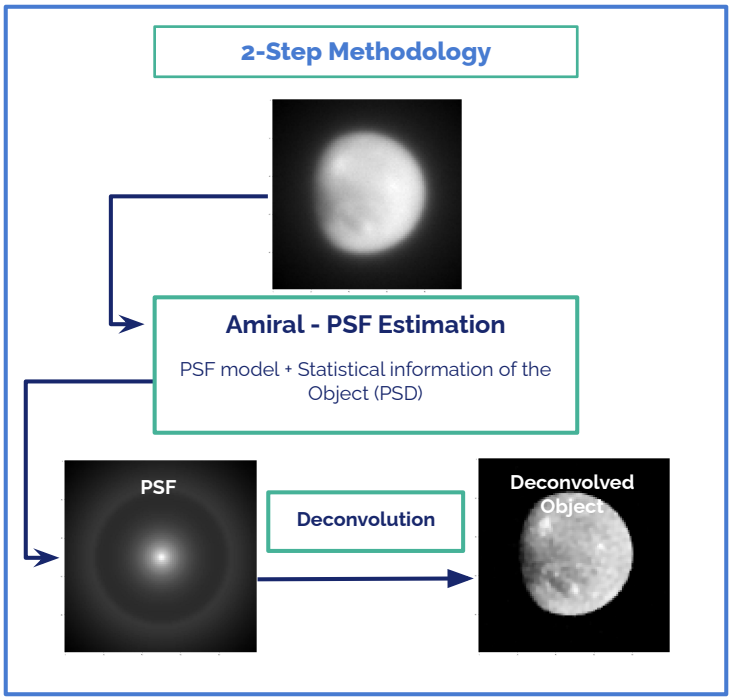

Figure 3. Schematic showing how to perform blind deconvolution with our pipeline. It is separated into two steps: 1. PSF estimation with amiral, 2. deconvolution using the PSF generated from the estimated PSF parameters.

with the estimated PSF, shown in fig. 3. We apply a marginal estimator to separate the object o from the rest of the parameters by integrating variables over their probability,

$$P(\gamma|i) = \int P(i|o,\gamma)P(\gamma)P(o)do \tag{4}$$

where γ represents the PSF parameters. Computing the marginalisation integral requires the following assumption : Gaussian probability for the object, stationary Gaussian white noise and the covariance matrix R_o. Therefore, the probability function is:

$$P(i|\gamma) \propto \frac{1}{\sqrt{\det R_i}} \exp^{-\frac{1}{2}(i-i_m)^t {R_i}^{-1}(i-i_m)}, \tag{5}$$

where R_i is the image covariance matrix and i_m is the convolution of estimated PSF and the mean object. With the assumption of the Gaussian stationary noise, the image covariance matrix is

$$R_i = H_\gamma R_o {H_\gamma}^t + \left\langle {\sigma_n}^2 \right\rangle I_d, \tag{6}$$

where $< \sigma_n^2 >$ is the average noise variance of the pixels, I_d is the identity matrix and H_γ is the convolution operator. The marginal criterion J can be written in the Fourier domain by taking the logarithm of the $P(\gamma|i)$,[5]

$$\begin{aligned} J_{marg}(\gamma; S_{obj}, <\sigma_n^2>) = \frac{1}{2}\sum \ln\left(S_{obj}|\tilde{h_\gamma}|^2 + <\sigma_n^2>\right) \\ + \frac{1}{2}\sum \frac{|\tilde{i} - \tilde{h}\tilde{o_m}|^2}{S_{obj}|\tilde{h}|^2 + <\sigma_n^2>} - \ln(\gamma), \end{aligned} \tag{7}$$

where S_{obj} is the PSD of the object and $\ln(\gamma)$ represents the precursory information on the PSF parameters, if there is any. Eq. 7 requires an object PSD and the noise statistics. For the object PSD, we propose using a

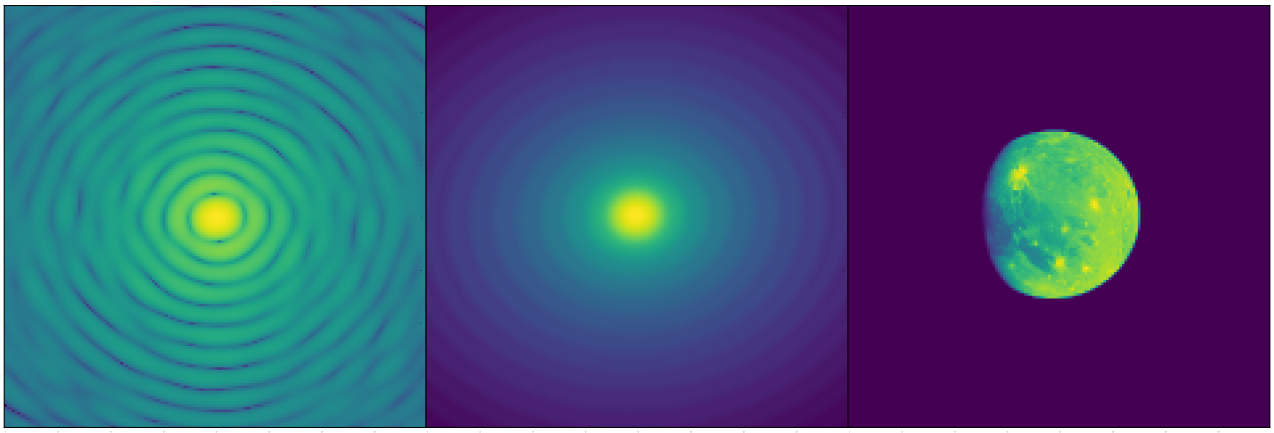

Figure 4. Demonstration of the object PSD model, all visualised with the same array size. Left: the PSD of the object, middle: PSD object generated from our model, right: the object.

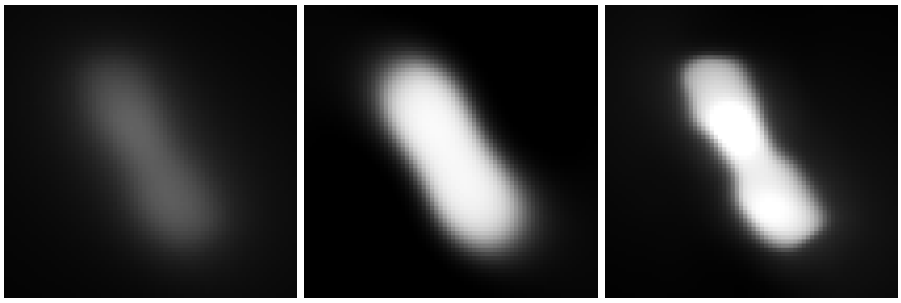

Figure 5. Left: VLT-SPHERE Observation of Kleopatra. Mid: Deconvolution using Conan PSD model.[7] Right: Deconvolution using PSF estimated with elliptical PSD model. The scale of all images is set to the same level.

Fourier-based formulation, which is effectively the Fourier transform of an ellipse. Elliptical PSD representation is chosen because the shape of the extended targets we observe are irregular, and results in elongated features in their PSDs.

Fig. 4 illustrates the PSD of the object, fitted PSD generated by our model, the object and the chosen ellipse. The global features from fitted PSD, for instance, annuli, the core and the eccentricity are well-matched with the object PSD. When comparing the chosen ellipse and the object, we notice that the ellipse is two times bigger than the object. As there is a filtering process when calculating the final object PSD, over-estimation in size may be required. The benefit of this model is that initial guesses of the PSD parameters can be obtained directly from the image PSD, given that the image PSD is the convolution product between the object and the PSF, added with noise.

We further apply our PSF estimation method with the improved object model to real observations. Instead of using Moffat PSF to recover the asteroid, we reprocess the published data with our improved pipeline. Before modifying the object PSD model, we fail to retrieve this dog-bone-shaped asteroid with the marginal estimator. One can perform deconvolution with different parameters using the model of their choice (e.g Moffat, Gaussian).

The drawback is that the post-processing can be complex because it involves many trials and errors, and intensive visual inspections are compulsory. Comparing the output using Moffat PSF in fig. 5 (right) to the deconvolved object using blind deconvolution with an improved PSD model (mid), the shape of the asteroid is almost identical. Also, the middle output demands less human labour because only a couple of PSF estimations are needed to get the optimal set of variables. We free most of the PSF and object PSD for minimisation. The output is then transferred and generates a PSF to recover the object. We present that our PSF estimation method can perform a robust estimation without having several demanding and complicated post-processing and visual inspections.

5. CONCLUSION AND PERSPECTIVES

We presented the general requirement for deconvolution by studying deconvolved objects with 225 different PSFs. Indeed, deconvolution is sensitive towards the PSFs, but the required precision is quite relaxed. The tolerance is higher than our anticipation. Based on the requirement we find, our tool is able to deliver the results within the range. Then we improve the blind deconvolution by introducing a Fourier-based elliptical PSD model. A more realistic object model enables us to apply blind deconvolution to Kleopatra observations from VLT-SPHERE. The deconvolved object with our method is comparable with published results,[10] while we provide a more robust and straightforward blind deconvolution method for extended targets in the Solar System. Our successful application to on-sky data proves that we can perform blind deconvolution with a wider range of targets and system configurations. Consequently, we have started to study the possibility of blind deconvolution on hyper-spectral data cube with prior information.

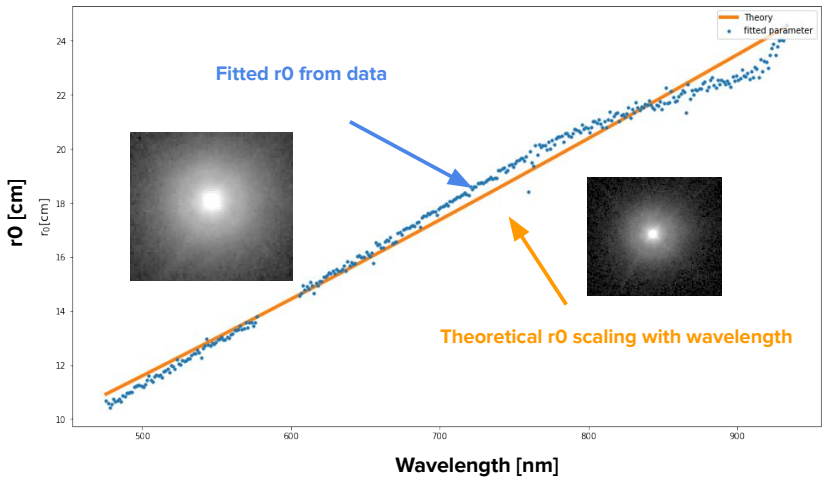

Figure 6. Fitted $r0$ from MUSE-NFM PSF in blue dots with the theoretical $r0$ scaling with wavelength in orange line. Here we take one PSF as an example to demonstrate the possible relationship between $r0$ and wavelength. The variation of fitted $r0$ as a function of wavelength agrees with the scaling. In longer wavelengths, the fitted $r0$ deviates from the theoretical relationship.

We can start with the evolution of the PSF as a function of the wavelength. Fig. 6 shows that the fitted $r0$ agrees with the theoretical scaling in wavelength. A PSF archive can help to demonstrate this wavelength scaling for other parameters. Utilising the scaling means fewer estimations are made to deconvolve the whole data cube, cutting down the computational time and resources when processing hyper-spectral data. Therefore, we are working on incorporating the wavelength variation into the criterion. Another approach to improve PSF estimation is to use all available information from the AO telemetry as a prior. The AO telemetry data provides insights into observing conditions. These could help us to put a constraint on the output PSF. In addition, further work is needed if we would like to introduce a different class of extended objects, for instance, galaxies with different topologies. Extending the blind deconvolution to handle a more diverse class of objects either will need additional inputs from the astronomical model, or one may try exploring machine learning methods to build a more complex model to help us improve blind deconvolution.

ACKNOWLEDGMENTS

This work benefited from the support of the the French National Research Agency (ANR) with WOLF (ANR-18-CE31-0018), APPLY (ANR-19-CE31-0011) and LabEx FOCUS (ANR-11-LABX-0013); the Programme Investissement Avenir F-CELT (ANR-21-ESRE-0008), the Action Spécifique Haute Résolution Angulaire (ASHRA) of CNRS/INSU co-funded by CNES, the ECOS-CONYCIT France-Chile cooperation (C20E02), the ORP H2020 Framework Programme of the European Commission's (Grant number 101004719) and STIC AmSud (21-STIC-09).

REFERENCES

[1] Davies, R. and Kasper, M., "Adaptive Optics for Astronomy," **50**, 305–351 (Sept. 2012).

[2] Fétick, R. J., Jorda, L., Vernazza, P., Marsset, M., Drouard, A., Fusco, T., Carry, B., Marchis, F., Hanuš, J., Viikinkoski, M., Birlan, M., Bartczak, P., Berthier, J., Castillo-Rogez, J., Cipriani, F., Colas, F., Dudziński, G., Dumas, C., Ferrais, M., Jehin, E., Kaasalainen, M., Kryszczynska, A., Lamy, P., Le Coroller, H., Marciniak, A., Michalowski, T., Michel, P., Mugnier, L. M., Neichel, B., Pajuelo, M., Podlewska-Gaca, E., Santana-Ros, T., Tanga, P., Vachier, F., Vigan, A., Witasse, O., and Yang, B., "Closing the gap between Earth-based and interplanetary mission observations: Vesta seen by VLT/SPHERE," **623**, A6 (Mar. 2019).

[3] Mugnier, L. M., Fusco, T., and Conan, J.-M., "Mistral: a myopic edge-preserving image restoration method, with application to astronomical adaptive-optics-corrected long-exposure images," *J. Opt. Soc. Am. A* **21**, 1841–1854 (Oct 2004).

[4] Fétick, R. J. L., Mugnier, L. M., Fusco, T., and Neichel, B., "Blind deconvolution in astronomy with adaptive optics: the parametric marginal approach," **496**, 4209–4220 (Aug. 2020).

[5] Blanco, L. and Mugnier, L. M., "Marginal blind deconvolution of adaptive optics retinal images," *Optics Express* **19**, 23227 (Nov. 2011).

[6] Fétick, R. J. L., Fusco, T., Neichel, B., Mugnier, L. M., Beltramo-Martin, O., Bonnefois, A., Petit, C., Milli, J., Vernet, J., Oberti, S., and Bacon, R., "Physics-based model of the adaptive-optics-corrected point spread function. Applications to the SPHERE/ZIMPOL and MUSE instruments," **628**, A99 (Aug. 2019).

[7] Conan, J.-M., Mugnier, L. M., Fusco, T., Michau, V., and Rousset, G., "Myopic deconvolution of adaptive optics images by use of object and point-spread function power spectra," **37**, 4614–4622 (July 1998).

[8] NASA, "See the first images nasa's juno took as it sailed by ganymede," (2021).

[9] Roddier, F., "The effects of atmospheric turbulence in optical astronomy," *Progess in Optics* **19**, 281–376 (Jan. 1981).

[10] Marchis, F., Jorda, L., Vernazza, P., Brož, M., Hanuš, J., Ferrais, M., Vachier, F., Rambaux, N., Marsset, M., Viikinkoski, M., Jehin, E., Benseguane, S., Podlewska-Gaca, E., Carry, B., Drouard, A., Fauvaud, S., Birlan, M., Berthier, J., Bartczak, P., Dumas, C., Dudziński, G., Ďurech, J., Castillo-Rogez, J., Cipriani, F., Colas, F., Fetick, R., Fusco, T., Grice, J., Kryszczynska, A., Lamy, P., Marciniak, A., Michalowski, T., Michel, P., Pajuelo, M., Santana-Ros, T., Tanga, P., Vigan, A., Witasse, O., and Yang, B., "(216) Kleopatra, a low density critically rotating M-type asteroid," **653**, A57 (Sept. 2021).